Trimmed Aperture Corner Reflector for Angle-Selective Chipless RFID

Tatsuya Iizuka [iD], Naoko Kosaka, Masaki Hisada, Yoshihiro Kawahara [iD], *Member, IEEE*,
and Takuya Sasatani [iD], *Member, IEEE*

Abstract—This letter presents trimmed aperture corner reflectors (CRs) for assigning angle selectivity to chipless radio frequency identification (RFID) tags. This angle selectivity can benefit the landmark use of CR-based tags by exhibiting different signals in each direction, which enables infrastructure-to-device communication with rich context. The key idea of this work is to subtract retroreflections in unwanted directions by partially trimming the aperture of CRs, allowing control over the radar crosssection (RCS) when looked at from different angles. We developed a geometric analysis based on the effective area of CRs to determine the appropriate aperture trimming for the desired angular characteristics. This method can append direction selectivity to various CR-based chipless RFID tags. We demonstrate a trimmed CR-based spatially coded chipless RFID that can present different 4-bit IDs in three different directions while maintaining a large RCS of 1.80 dBsm. The proposed method can artificially code the selective reflections in passive reflectors and is suitable for the applications requiring large detectability, such as outdoor landmarks and signs.

Index Terms—Chipless radio frequency identification (RFID), corner reflector (CR), millimeter-wave radar (mmWave), radar crosssection (RCS).

I. INTRODUCTION

CORNER reflectors (CRs), known for their large radar crosssection (RCS) over a wide angle due to their retroreflective properties, have been extensively used in various applications, such as radar landmarks in the aviation and marine industries [1], [2], [3]. Leveraging this high visibility from radar devices, previous work has explored CR-based chipless radio frequency identification (RFID) technologies with frequency modulation via integration with frequency-selective surfaces [4], slot resonators [5], and dielectric resonators [6]. Since communication reliability in chipless RFID depends on the RCS of the tags [7], [8]. CR-based chipless RFID tags are expected to serve as outdoor landmarks to navigate vehicles like EVs and UAVs
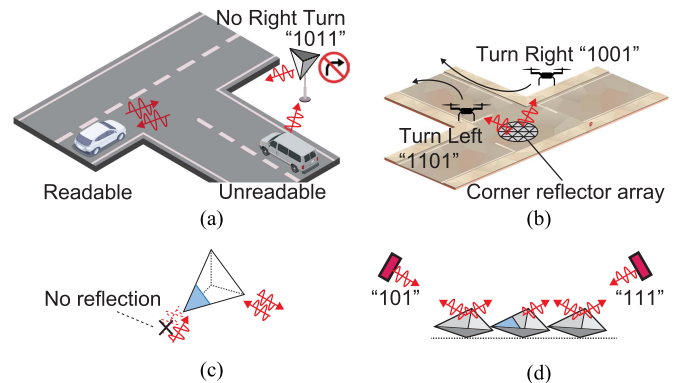
Fig. 1. Overview of application scenarios (a) and (b) and the proposed method (c) and (d). (a) Traffic signs signaling to vehicles coming from a specific direction. (b) UAV guidance systems for multiple directions. (c) Proposed trimmed aperture corner reflector for angle-selective reflection. (d) Spatial coding for sending different messages in each direction.

even in poor visibility conditions, such as in dark and foggy environments.

While the wide read angle of CRs is conducive to presenting a single ID to readers, it inhibits use cases that require angle selectivity, such as road signs of specific directions and multidirectional UAV guidance [see Fig. 1(a) and (b)]. To address this need, we propose a design method for trimming the aperture of CRs to control read angles exhibiting retroreflective properties [see Fig. 1(c) and (d)]. The key idea of this method is to subtract retroreflections in unwanted directions while preserving them in desired ones, based on the fact that the RCS can be computed via the projections of the characteristic CR geometry. We present a technique for determining how to trim the aperture of CRs when reflection in a certain direction is required. Experimental evaluations show controllable RCS for specific directions. This technique can be used in various CR-based chipless RFID systems. We demonstrate the feasibility of our method by designing an angle-selective spatial domain chipless RFID composed of six trimmed CRs that can independently present three different IDs in three directions.

II. TRIMMED APERTURE CORNER REFLECTOR

To design the angle dependency of the retroreflective feature of CRs, we introduce an RCS model based on CR geometry and extend the model for trimmed aperture CRs. We start by defining the coordinate system, as illustrated in Fig. 2(a). The CR is positioned such that its base (Point O) serves as the origin, the aperture plane ABC aligns parallel to the *XY*-plane, and vertex A
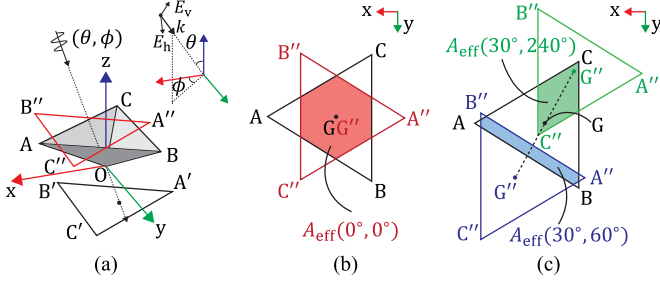
Fig. 2. Principle of retroreflection and effective area seen from different angles. (a) CR with a coordinate shows the retroreflection requirement for incident wave direction. The effective area can be computed as the overlap region of triangles ABC and A″B″C″. (b) and (c) Angle-dependent effective area A_{eff} when $(\theta, \phi) = (0°, 0°)$, $(30°, 60°)$, and $(0°, 240°)$.
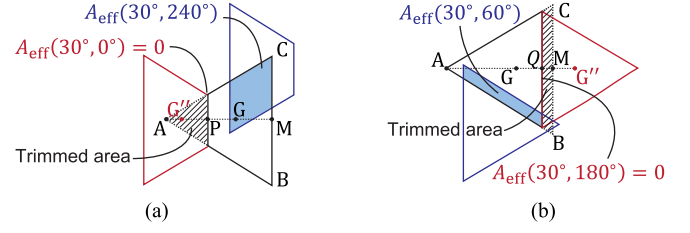

Fig. 3. Trimmed apertures of CRs and their effective area. The trimmed areas were determined based on (5) and (6). (a) Vertex-trimmed aperture that has an effective area of 0 for $(\theta, \phi) = (30°, 0°)$. (b) Edge-trimmed aperture that has an effective area of 0 for $(\theta, \phi) = (30°, 180°)$. The apertures in both (a) and (b) maintain large effective areas for other azimuth directions ϕ.

resides in the *XZ*-plane. The incident wave's direction is denoted by θ and ϕ. When a CR side length of $a(= \text{OA} = \text{OB} = \text{OC})$ is sufficiently small compared with the incident wavelength λ, the geometric approximation holds and the RCS σ can be expressed as a function of the effective area A_{eff} as follows [9]:

$$\sigma(\theta, \phi) = \frac{4\pi}{\lambda^2} A_{\text{eff}}^2(\theta, \phi). \tag{1}$$

The effective area is the region where the incoming rays undergo triple reflection within the cavity, causing retroreflection, and is generally smaller than the aperture area. This condition is equivalent to when the rays pass through triangles ABC and A′B′C′ simultaneously, with A′B′C′ being the origin-symmetric triangle of ABC [see Fig. 2(a)]. To facilitate visual understanding, we cast triangle A′B′C′ along the incident wave vector onto the ABC plane to obtain triangle A″B″C″ so that the effective area can be computed as the overlap region of triangles ABC and A″B″C″ as follows:

$$A_{\text{eff}}(\theta, \phi) = \iint_D dx\, dy, D : (x, y) \in (\triangle ABC \cap \triangle A''B''C'').\tag{2}$$

When the centers of gravity of triangles ABC and A″B″C″ are denoted as G and G″, their coordinates can be represented as follows, indicating that A_{eff} varies with the incident angle:

$$(\text{G}_x, \text{G}_y) = (0, 0) \tag{3}$$

$$(\text{G}''_x, \text{G}''_y) = \left(\frac{2}{\sqrt{3}} a \tan\theta \cos\phi, \frac{2}{\sqrt{3}} a \tan\theta \sin\phi \right). \tag{4}$$

Next, we extend the analysis to trimmed aperture CRs. Fig. 2(c) shows that the area near the tip of each triangle contributes significantly to the effective area seen from the vertex direction. Thus, the RCS seen from a particular vertex direction can be reduced by trimming one end of the aperture triangle, resulting in a vertex-trimmed CR, shown in Fig. 3(a). Similarly, Fig. 3(b) shows an edge-trimmed CR that aims to reduce the RCS seen from the edge direction. To simplify the design process, we introduce the following ratios expressing the amount of trimming for each design variation: $s_{\text{v}} = \text{AP/AM}$ for the vertex-trimmed CR [see Fig. 3(a)], and $s_{\text{e}} = \text{QM/AM}$ for the edge-trimmed CR [see Fig. 3(b)]. The smallest $s_{\text{v}}^{\text{opt}}$ and $s_{\text{e}}^{\text{opt}}$ ratios, which show an effective area of zero in the suppressed direction, meet the condition of $\text{PG} = \text{PG}'' = \frac{1}{2} \cdot |\text{GG}''|_{\phi=0°}$ and $\text{QG} = \text{QG}'' = \frac{1}{2} \cdot |\text{GG}''|_{\phi=180°}$, respectively. Thus, $s_{\text{v}}^{\text{opt}}$

and $s_{\text{e}}^{\text{opt}}$ can be solved as

$$s_{\text{v}}^{\text{opt}}(\theta) = \frac{\text{AG} - \text{PG}}{\text{AM}} = \frac{2 - \sqrt{2}\tan\theta}{3}, (\theta < 54.7°) \tag{5}$$

$$s_{\text{e}}^{\text{opt}}(\theta) = \frac{\text{MG} - \text{QG}}{\text{AM}} = \frac{1 - \sqrt{2}\tan\theta}{3}, (\theta < 35.2°). \tag{6}$$

III. SIMULATION-BASED ANALYSIS

To validate the vertex- and edge-trimmed CR design, we evaluated the angle dependency of the RCS calculated using method of moments (MoM) simulations using HFSS-IE solver. We set the operating frequency to $f_{\text{c}} = 79$ GHz, corresponding to a wavelength of 3.8 mm, and the side length to $a = 45$ mm. We optimized the trimming ratios for $\theta = 30°$, resulting in $s_{\text{v}} = s_{\text{v}}^{\text{opt}}(30°) = 0.39$ for the vertex-trimmed CR and $s_{\text{e}} = s_{\text{e}}^{\text{opt}}(30°) = 0.06$ for the edge-trimmed CR, respectively.

Fig. 4 shows the RCS for vertical polarization when varying the elevation angle to examine whether the reflection is effectively suppressed or preserved around $\theta = 30°$ as intended without affecting reflections at other angles. In both cases, the blue lines show a design in which the reflection is preserved, the red lines show a design in which the reflection is suppressed, and the dotted green lines show the results for a "nontrimmed" CR. The RCS is below 15 dBsm in ranges of approximately $20°$–$45°$ for the vertex-trimmed case [see Fig. 4(a)] and $25°$–$32.5°$ for the edge-trimmed case [see Fig. 4(b)], demonstrating their tolerance to the elevation angle. The RCS peak appearing at $\theta = 35°$ in Fig. 4(b) is not a retroreflection but an exceptional reflection caused when the incident angle is perpendicular to the CR cavity plane [10]. It is known that this exceptional reflection can be
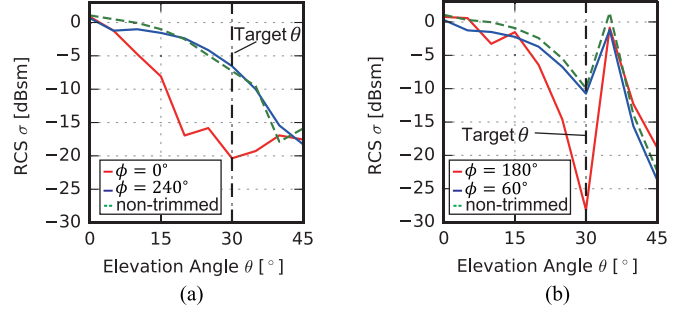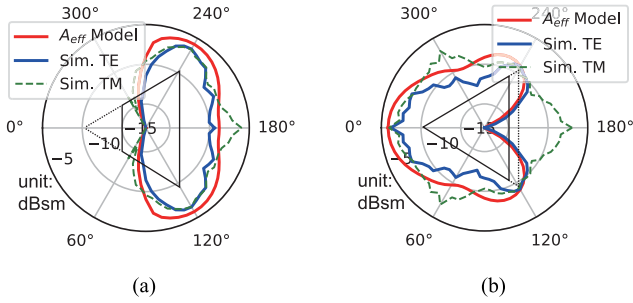

Fig. 4. RCS of (a) vertex- and (b) edge-trimmed aperture CRs at different elevation angles θ with the corresponding azimuth angles shown in Fig. 3.

Fig. 5. RCS of (a) vertex- and (b) edge-trimmed aperture CRs at different azimuth angles ϕ with θ fixed at $30°$. The unit is dBsm. The RCS evaluations were derived using the analytical model A_{eff} and MoM simulations with TE and TM modes.

TABLE I
RADAR MEASUREMENT PARAMETERS

Parameter	Value
Carrier frequency	77 GHz
Bandwidth (range resolution)	4 GHz (37.5 mm)
Time window	110 μs
Antenna beamwidth	$14°$ (elev.), $28°$ (azim.)
Polarization	Vertical polarization (TE)

adjusted by changing the facing direction of the CR and can be avoided when designed for a specific application scenario [11].

Next, we calculated the RCS characteristics at varying azimuth angles ϕ with fixed $\theta = 30°$ using the analytical model [see (1)–(4)] and MoM simulations to investigate the vertical [transverse electric (TE)] and horizontal transverse magnetic (TM)] polarizations of the incident waves (see Fig. 5). In TE mode, the analytical model and MoM simulation were in good agreement and the two optimal trimming ratios $s_{\text{e}}^{\text{opt}}$ and $s_{\text{v}}^{\text{opt}}$ provided complete suppression of reflection in a specific direction, such as $\phi = 0°$ [see Fig. 5(a)] and $\phi = 180°$ [see Fig. 5(b)], while maintaining the strong reflection in other azimuth directions. The RCS values obtained from the analytical model were slightly higher than those obtained from TE mode, but this is reasonable, considering that the actual effective area was reduced by the effect of the wavelength.

On the other hand, a mismatch with the model appeared in TM mode at $\phi = 60°, 180°$, and $300°$. This is because of a resonant response on the edges parallel to the electric field vectors, which the geometric analysis does not take into account. For applications, this requires considering the installation orientation or using multiple radar front ends with different polarizations, which is feasible in most cases due to the small form factor and low cost of millimeter-wave (mmWave) radar modules. Because straightforward countermeasures exist for this limitation, we proceeded considering only TE mode.

IV. MEASUREMENT OF A TRIMMED CORNER REFLECTOR

We fabricated a trimmed CR with $s_{\text{v}} = 0.39$ in the vertex direction and $s_{\text{e}} = 0.06$ in the edge direction. Fig. 6 shows the six types of trimmed CR fabricated by hollowing out a triangular prism with a height of 30 mm and a width of 75 mm. We named each type according to the direction and number of intended retroreflections (for example, E2 stands for retroreflection in the directions of two edges). The measurements were conducted using a 79 GHz mmWave frequency-modulated continuous-wave (FMCW) radar positioned 5.7 m away. We used an IWR 1443-based evaluation module [12]. Table I gives the key measurement parameters. To obtain the actual RCS with the FMCW radar, we used a large CR with 20 dBsm as the reference based on previously developed RCS measurement methods [9], [13], [14]. The blue line shows the MoM simulation values, and the red dots indicate the measured RCS values at $\theta = 30°$, which were in good agreement with the simulation values. Notably, this result

confirmed the successful control over the presence or absence of reflections at six distinct azimuth angles and the feasibility of the proposed method for angle-selective chipless RFIDs.

V. ANGLE-SELECTIVE SPATIAL CODING

To demonstrate the utility of our trimmed CR methodology, we developed a spatially modulated chipless RFID tag system [15] that can be designed to present different bit sequences in three azimuthal directions ($\phi = 0°, 120°$, and $240°$). Fig. 7 shows our tag system design, which arranges 24 trimmed CRs on a plane that form spatial electromagnetic reflectivity patterns. The FMCW radars can detect these patterns as range power profiles in a slant range [16], which are later converted to bit patterns. The FMCW radar detects the superposition of the reflection of each CR through the intermediate frequency (IF) signal $s(t)$. The amplitude, frequency, and phase of the reflection added by each CR depend on its RCS and position. This $s(t)$ is expressed by the following equation when N reflectors exist on the tag:

$$s(t) = \sum_{i=1}^{N} a_i \cdot e^{j2\pi f_i t} + w(t) \tag{7}$$

$$f_i = \frac{1}{T} \cdot \frac{d_i}{R_{\text{res}}} = \frac{2B}{cT} \cdot d_i \tag{8}$$

$$a_i = \left[\frac{P_{\text{t}} G^2 \lambda^2}{(4\pi)^3 d_i^4} \cdot \sigma(\theta_{\text{e}}, \phi_{\text{e}}) \right]^{\frac{1}{2}} \tag{9}$$

where d_i is the distance between the radar and the ith reflector ($1 \le i \le N$), R_{res} is the radar distance resolution with range fast Fourier transform (range-FFT), B is the chirp bandwidth of the FMCW radar, T is the chirp duration, c is the speed of light, G is the radar antenna gain, P_{t} is the transmission power, and $w(t)$ is a white noise signal. Our design superimposes bit sequences on the range power profile, which is calculated by applying range-FFT to $s(t)$. This transforms the 2-D reflective properties on the plane into a 1-D distance intensity distribution. When the radar is far from the tag, the reflectors placed orthogonally to the read direction add up in the readout, forming a single bit.

Next, we show how to arrange the trimmed CRs when the desired bit sequences for three directions ($\phi = 0°, 120°$, and $240°$) are given. The necessary type of trimmed CR in each position can be uniquely determined based on the presence or absence of reflection in the three directions. For instance, the CR at the red triangle position in Fig. 7 requires reflection only in the $\phi = 0°$ and $\phi = 120°$ directions, so V2 is appropriate. Similarly, E1 is appropriate in the blue triangle position.

Finally, we read out our tag using the FMCW radar from different angles. Fig. 8 shows the measurement setup and the acquired range power profile. The mmWave radar was attached
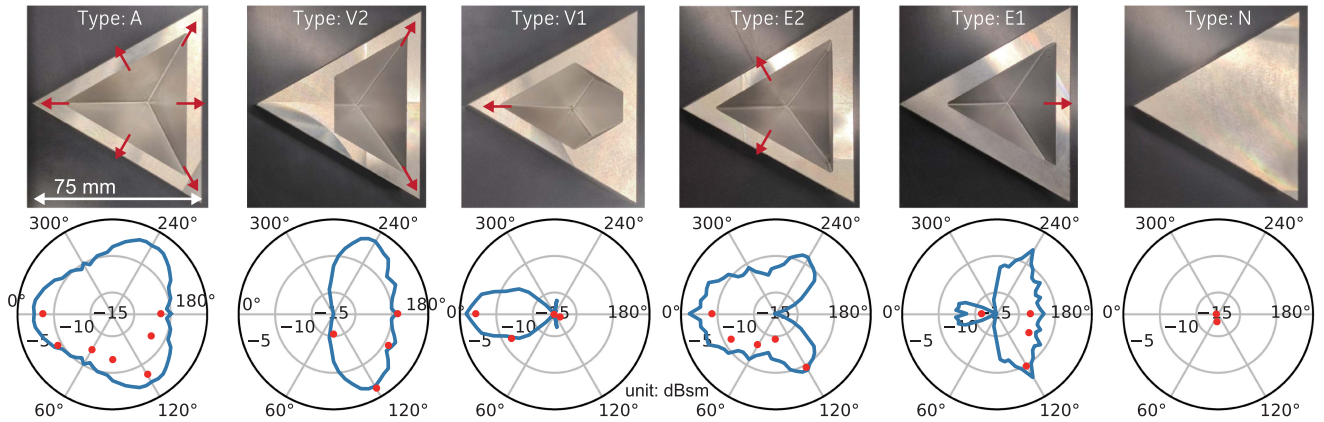
Fig. 6. Fabricated CRs with trimmed apertures and their RCS characteristics in dBsm. Six types of trimmed CRs (A, V2, V1, E2, E1, and N) were made to control the presence of reflection in the **Vertex** and **Edge** directions. The red arrows in the top images indicate the directions in which there are significant reflections. The bottom graphs show the measured RCS values (red dots) and simulated values (blue lines) for fixed $\theta = 30°$.
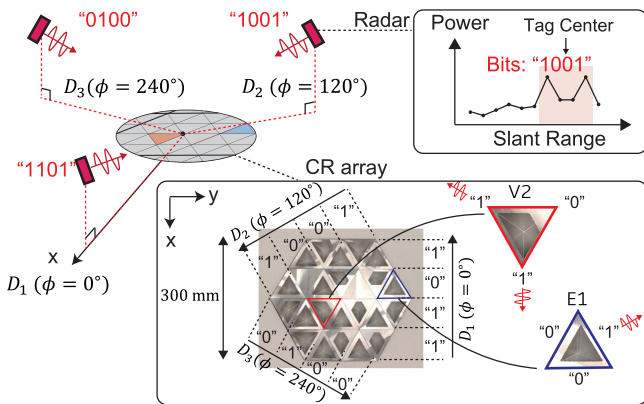

Fig. 7. Overview of spatial coding interpretable by a slant range radar. The trimmed CRs were placed on a plane. The CR arrangement presents different 4bit sequences in three directions (D_1, D_2, and D_3).
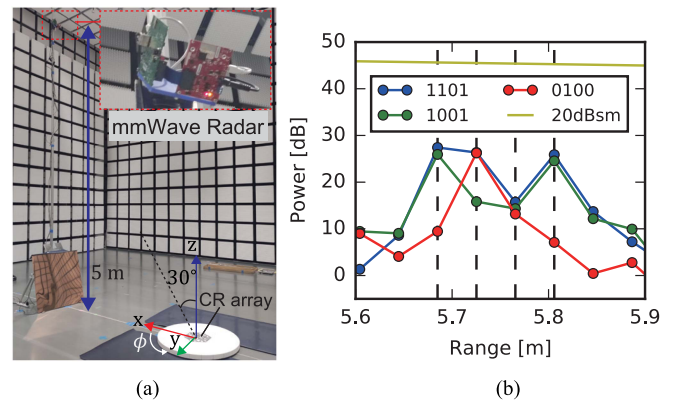

Fig. 8. Experimental setup (a) and measurement results (b). (a) mmWave radar was mounted on top of a pole, and the CRs were arranged as shown in Fig. 7. (b) Readout results of the directional chipless RFID from different azimuth angles ϕ. The encoded bit sequences "1101," "1001," and "0100" were correctly read out for each direction.

to the tip of a 5 m pole positioned in such a way that the incident elevation angle θ was $30°$ and the radar antenna was directed toward the center of the tag. The radar parameters were set as given in Table I, making the ground distance resolution $R_{res} \cdot \sin\theta$ same as the width of the fabricated CRs (75 mm). Fig. 8(b) shows that the radar acquired the designed bit sequences "1101," "1001," and "0100" for read angles $\phi = 0°$, $120°$, and $240°$, respectively. The reflected power of bit "1" was greater than 25 dB, that of bit "0" was less than 15 dB, and the averaged signal-to-noise ratio (SNR) calculated as the power ratio of bits "1" and "0" was 11.2 dB, which allows reliable bit detection. This was lower than the actual average RCS difference of 15.9 dB obtained from the sum of the square roots of each angle-dependent RCS (see Fig. 6). This deviation can be attributed to a decrease in amplitude stemming from the phase variation of each reflected wave in superposition in (7) and (8) and spectral leakage in the FFT-based analysis [17].

To examine the RCS, we measured a reference CR with a 20 dBsm RCS that had an IF power of 47.85 dB received at a distance of 5 m from the radar. The yellow line in Fig. 8(b) shows the reflected power corresponding to 20 dBsm at each distance, taking distance attenuation into account. The received

power of bit "1" at the first bit of the sequence for the direction D_1 ($\phi = 0°$) was 27.41 dB, corresponding to a large RCS of 1.80 dBsm, thereby confirming that the tag maintained strong reflection while adding angle selectivity.

VI. Conclusion

This letter presents a method for angle selectivity in CRs via aperture trimming that enables enriched communication in chipless RFIDs. Another critical advantage is that the presented spatial coding approach lowers the barriers to implementation by using mmWave radars developed for automotive and other industrial applications. The suggested geometric model has the potential to modify apertures to expand the maximum reflective angles, for example, by deforming the aperture shape so that the triangle is vertically elongated [11]. The method's foundation, applicable to common CRs, broadens its applicability to various frequency bands and holds promise for incorporating angle selectivity into existing CR-based chipless RFIDs, including frequency coding [4], [5], [6].

REFERENCES

[1] K. Sarabandi and T.-C. Chiu, "Optimum corner reflectors for calibration of imaging radars," *IEEE Trans. Antennas Propag.*, vol. 44, no. 10, pp. 1348–1361, Oct. 1996.

[2] Y. Zhou, C. Li, L. Ma, M. Y. Yang, and Q. Liu, "Improved trihedral corner reflector for high-precision SAR calibration and validation," in *Proc. IEEE Geosci. Remote Sens. Symp.*, 2014, pp. 454–457.

[3] W. He et al., "Investigation of radar cross-section reduction for dihedral corner reflectors based on camouflage grass," *IEEE Antennas Wireless Propag. Lett.*, vol. 20, no. 12, pp. 2447–2451, Dec. 2021.

[4] A. Jiménez-Sáez et al., "Frequency selective surface coded retroreflectors for chipless indoor localization tag landmarks," *IEEE Antennas Wireless Propag. Lett.*, vol. 19, no. 5, pp. 726–730, May 2020.

[5] K. R. Brinker and R. Zoughi, "Corner reflector based misalignment-tolerant chipless RFID tag design methodology," *IEEE J. Radio Freq. Identif.*, vol. 5, no. 1, pp. 94–105, Mar. 2021.

[6] A. A. Abbas, M. El-Absi, A. Abuelhaija, K. Solbach, and T. Kaiser, "Corner reflector tag with RCS frequency coding by dielectric resonators," *Microw., Antennas Propag.*, vol. 15, no. 6, pp. 560–570, 2021.

[7] M. Borgese, S. Genovesi, G. Manara, and F. Costa, "Radar cross section of chipless RFID tags and BER performance," *IEEE Trans. Antennas Propag.*, vol. 69, no. 5, pp. 2877–2886, May 2021.

[8] W.-J. Liao, Y.-C. Hou, C.-C. Tsai, T.-H. Hsieh, and H.-J. Hsieh, "Radar cross section enhancing structures for automotive radars," *IEEE Antennas Wireless Propag. Lett.*, vol. 17, no. 3, pp. 418–421, Mar. 2018.

[9] M. I. Skolnik, *Radar Handbook*. New York, NY, USA: McGraw-Hill, 2008.

[10] E. F. Knott, J. F. Schaeffer, and M. T. Tulley, *Radar Cross Section*. Raleigh, NC, USA: SciTech, 2004.

[11] P. Dheenathayalan, M. C. Cuenca, P. Hoogeboom, and R. F. Hanssen, "Small reflectors for ground motion monitoring with in SAR," *IEEE Trans. Geosci. Remote Sens.*, vol. 55, no. 12, pp. 6703–6712, Dec. 2017.

[12] Texas Instruments, "TI IWR1443 single-chip 76-GHz to 81-GHz mmWave sensor evaluation module." Accessed on: Jun. 13, 2023. [Online]. Available: https://www.ti.com/tool/IWR1443BOOST

[13] S. Lee, S. Kang, S.-C. Kim, and J.-E. Lee, "Radar cross section measurement with 77 GHz automotive FMCW radar," in *Proc. IEEE 27th Annu. Int. Symp. Pers., Indoor, Mobile Radio Commun.*, 2016, pp. 1–6.

[14] D. A. Robertson, R. J. Middleton, and D. G. Macfarlane, "A 94 GHz FMCW instrumentation radar," in *Proc. Joint 32nd Int. Conf. Infrared Millimeter Waves, 15th Int. Conf. Terahertz Electron.*, 2007, pp. 919–921.

[15] D. H. Nguyen, M. Zomorrodi, and N. C. Karmakar, "Spatial-based chipless RFID system," *IEEE J. Radio Freq. Identif.*, vol. 3, no. 1, pp. 46–55, Mar. 2019.

[16] L. M. Arjomandi, G. Khadka, and N. C. Karmakar, "mm-Wave chipless RFID decoding: Introducing image-based deep learning techniques," *IEEE Trans. Antennas Propag.*, vol. 70, no. 5, pp. 3700–3709, May 2022.

[17] A. V. Oppenheim and R. W. Schafer, *Discrete-Time Signal Processing*. Noida, India: Pearson Educ., 1999.